

The Hydromechanical Interplay in the Simplified Three-dimensional Limit Equilibrium Analyses of Unsaturated Slope Stability

Sitarenios, P. & Casini, F.

Published PDF deposited in Coventry University's Repository

Original citation:

Sitarenios, P & Casini, F 2021, 'The Hydromechanical Interplay in the Simplified Three-dimensional Limit Equilibrium Analyses of Unsaturated Slope Stability', *Geosciences*, vol. 11, no. 2, 73.

<https://dx.doi.org/10.3390/geosciences11020073>

DOI 10.3390/geosciences11020073

ESSN 2076-3263


Publisher: MDPI

Copyright: © 2021 by the authors. Licensee MDPI, Basel, Switzerland.

This article is an open access article distributed under the terms and conditions of the Creative Commons Attribution (CC BY) license (<http://creativecommons.org/licenses/by/4.0/>).

Article

The Hydromechanical Interplay in the Simplified Three-Dimensional Limit Equilibrium Analyses of Unsaturated Slope Stability

Panagiotis Sitarenios^{1,*} and Francesca Casini² ¹ School of Energy, Construction and Environment, Coventry University, Coventry CV1 5FB, UK² Dipartimento di Ingegneria Civile e Ingegneria Informatica (DICII), Università degli Studi di Roma "Tor Vergata", 00133 Roma, Italy; francesca.casini@uniroma2.it

* Correspondence: panagiotis.sitarenios@coventry.ac.uk

Abstract: This paper presents a three-dimensional slope stability limit equilibrium solution for translational planar failure modes. The proposed solution uses Bishop's average skeleton stress combined with the Mohr–Coulomb failure criterion to describe soil strength evolution under unsaturated conditions while its formulation ensures a natural and smooth transition from the unsaturated to the saturated regime and vice versa. The proposed analytical solution is evaluated by comparing its predictions with the results of the Ruedlingen slope failure experiment. The comparison suggests that, despite its relative simplicity, the analytical solution can capture the experimentally observed behaviour well and highlights the importance of considering lateral resistance together with a realistic interplay between mechanical parameters (cohesion) and hydraulic (pore water pressure) conditions.

Keywords: unsaturated slope; Ruedlingen field experiment; lateral resistance; limit equilibrium solution



Citation: Sitarenios, P.; Casini, F. The Hydromechanical Interplay in the Simplified Three-Dimensional Limit Equilibrium Analyses of Unsaturated Slope Stability. *Geosciences* **2021**, *11*, 73. <https://doi.org/10.3390/geosciences11020073>

Academic Editors: Jesus Martinez-Frias, Roberto Vassallo, Piernicola Lollino, Luca Comegna and Roberto Valentino
Received: 28 December 2020
Accepted: 25 January 2021
Published: 8 February 2021

Publisher's Note: MDPI stays neutral with regard to jurisdictional claims in published maps and institutional affiliations.



Copyright: © 2021 by the authors. Licensee MDPI, Basel, Switzerland. This article is an open access article distributed under the terms and conditions of the Creative Commons Attribution (CC BY) license (<https://creativecommons.org/licenses/by/4.0/>).

1. Introduction

It is well known that partial saturation can play a key role in stabilizing both natural and artificial slopes. The interparticle forces due to the formation of water menisci in the macrostructure and/or intermolecular forces due to absorptive and osmotic phenomena increase the shear strength of geomaterials, improving stability conditions. Loss of this beneficial contribution can significantly hinder stability conditions and trigger slope failures. A characteristic example is rainfall induced landslides which comprise one of the most common geotechnical failures [1–4].

Geotechnical failures occurring due to changes in hydraulic conditions highlight the significance that unsaturated soil mechanics can have in engineering problems. Unfortunately, despite its significant importance in many geotechnical problems, unsaturated soil mechanics still struggles today to find a place in everyday geotechnical practice. The reasons for this are usually related to the relative complexity of the material laws involved (i.e., water retention behaviour), the increased complexity of the required laboratory tests (i.e., suction controlled shear strength determination) and the lack of simple calculation tools accessible to everyday practitioners with fundamental knowledge of soil mechanics.

In this respect, the present paper presents and evaluates a simple slope stability limit equilibrium solution for translational failure modes. The proposed solution is initially obtained under two dimensions (2D) and it is later extended to three dimensions (3D) by additionally examining the potential development of shear strength along the sides of a sliding block with a finite lateral dimension. Similar solutions for unsaturated soil conditions exist in the international literature [1,5–8], where some refer to much simpler geometries (i.e., [6]) and others to more complex geometries requiring the use of the method of slices (i.e., [8]). Those closer to the mechanism adopted in this study usually involve assumptions which prevent them from remaining valid under saturated conditions,

especially when positive pore water pressures appear. The most common reasons are either the use of stress parameters which cannot recall Terzaghi's effective stress upon saturation (i.e., [7]) or assumptions with respect to the lateral in situ stress and its evolution with partial saturation, which are incompatible with classical soil mechanics principles (i.e., [1,5]).

The proposed stability solution is a natural extension of classical soil mechanics which is key in facilitating the adoption of such solutions in engineering practices [4]. To evaluate the proposed solution, this is applied to the analyses of a well instrumented field experiment where a slope failure was triggered by means of artificial rainfall—the Ruedlingen experiment [1,9]. This proves that, despite its simplicity, the proposed mechanism can very satisfactorily represent the experimentally observed behaviour both qualitatively and quantitatively. The presented discussion highlights the importance of considering the lateral development of the failure mechanism (3D) and of the natural transition to the saturated domain in capturing the behaviour.

2. A Slope Stability Limit Equilibrium Solution for Translational Modes in Unsaturated Soils

This section discusses the limit equilibrium stability calculation of a simple translational slope stability mechanism. Firstly, the assumed geometry is introduced and simple actions such as the weight of the sliding block are calculated. Then, the shear resistance along the failure plane is calculated considering the effect that partial saturation has on soil shear strength. Finally, the Factor of Safety (FoS) against failure is formulated by additionally considering the lateral resistance developing at the sides of a 3D failing soil block.

2.1. The Assumed Failure Mechanism

Figure 1 shows the assumed failure mechanism. A soil layer of thickness z rests on top of another material—the latter was assumed to be a priori of infinite strength. Both the soil surface and the interface between the two materials is described by two parallel planes with an inclination θ with the horizontal axis. The interface between the two materials acts as a potential failure surface (plane) and a simple translational failure mechanism develops where the upper layer tends to slide along the interface.

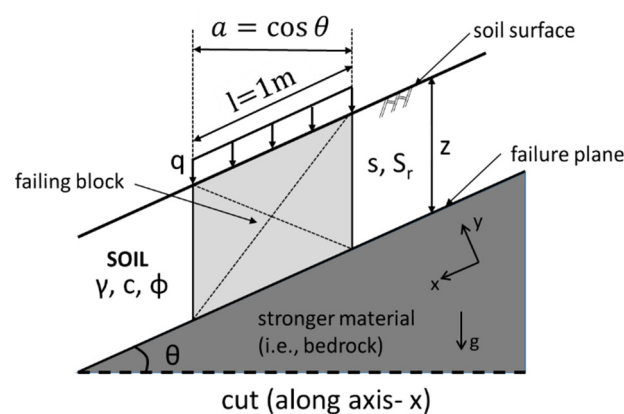


Figure 1. The analysed translational failure mechanism along a planar failure surface with slope θ .

To examine such a typical translational failure mechanism, we can isolate a block of soil with a length of $l = 1$ m along the x axis which is the one parallel to the failure plane as shown in Figure 1. To obtain an initial solution for a two-dimensional (2D) failure mechanism, an analyses per running meter was performed. The soil was assumed to be homogeneous and isotropic, while suction (s) and degree of saturation (S_r) were both assumed to be constant along the entire soil layer with no variation of depth in favour of simplicity. Moreover, for the sake of generality of the produced solution, a vertical surcharge equal to q was assumed on the surface of the soil.

The unit weight of the soil varies with degree of saturation (S_r) following Equation (1) as:

$$\gamma = \frac{G_s + e \cdot S_r}{1 + e} \cdot \gamma_w, \tag{1}$$

where G_s is the specific gravity and e the void ratio of the soil, while γ_w is the unit weight of the water usually assumed to be equal to $\gamma_w = 9.81 \text{ kN/m}^3$. Having defined the unit weight of the soil, the weight of the soil block (W) can be calculated and analysed as two components, W_x and W_y , along the x and y axes, respectively, as shown in Figure 2a:

$$W = \gamma \cdot z \cdot \cos\theta, \tag{2}$$

$$W_x = W \cdot \sin\theta = \gamma \cdot z \cdot \cos\theta \cdot \sin\theta, \tag{3}$$

$$W_y = W \cdot \cos\theta = \gamma \cdot z \cdot \cos^2\theta, \tag{4}$$

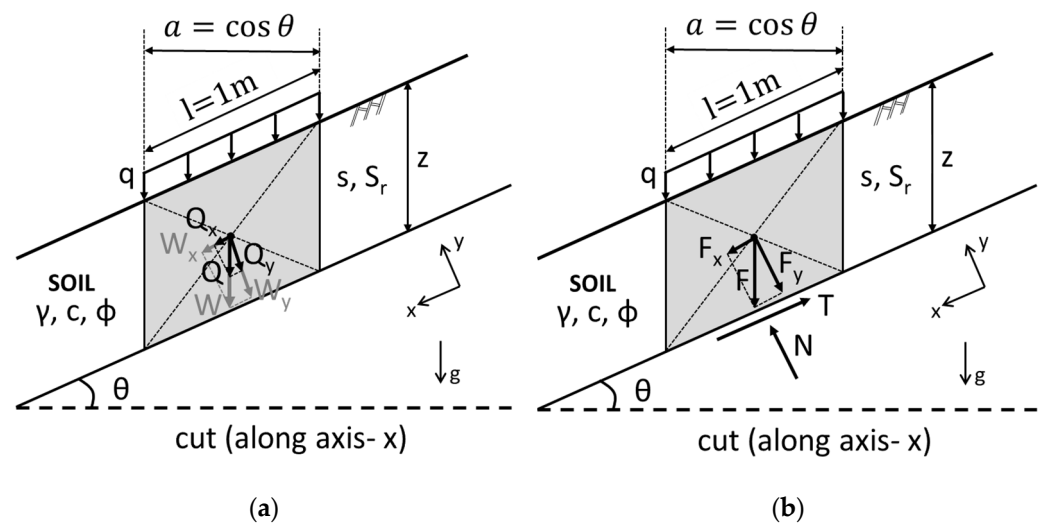


Figure 2. (a) Analyses of the weight of the block and of the applied surcharge; (b) equilibrium of the block along x axis (parallel to the failure plane) and y axis (perpendicular to the failure plane).

To further consider the effect of the uniform surcharge, we calculated the corresponding force (Q) and its two components, Q_x and Q_y , along the x and y axes, respectively, as shown in Figure 2a:

$$Q = q \cdot \cos\theta, \tag{5}$$

$$Q_x = Q \cdot \sin\theta = q \cdot \cos\theta \cdot \sin\theta, \tag{6}$$

$$Q_y = Q \cdot \cos\theta = q \cdot \cos^2\theta. \tag{7}$$

Finally, as portrayed in Figure 2b, the sum of the forces due to: (a) the weight of the soil block and (b) the surcharge is considered; initially on the x axis where F_x plays the role of the destabilizing action trying to slide the considered block along the failure surface,

$$F_x = Q_x + W_x = q \cdot \cos\theta \cdot \sin\theta + \gamma \cdot z \cdot \cos\theta \cdot \sin\theta = (q + \gamma z) \cos\theta \cdot \sin\theta, \tag{8}$$

and along the y -axis where F_y is equal to the reaction force from the bottom layer:

$$N = F_y = Q_y + W_y = q \cdot \cos^2\theta + \gamma \cdot z \cdot \cos^2\theta = (q + \gamma z) \cos^2\theta. \tag{9}$$

2.2. Shear Resistance under Unsaturated Conditions

The shear resistance at the interface is assumed to be entirely controlled by the shear strength parameters of the soil block and is described by the Mohr–Coulomb failure

envelope. The effect of partial saturation on shear strength is considered by using Bishop's (average) skeleton stress [10]. Bishop's average skeleton stress (σ') is calculated according to Equation (10) as the sum of the total stress (σ) plus suction ($s = -u_w$, assumed air pressure: $u_a = 0$); the latter is scaled for parameter χ .

$$\sigma' = \sigma + s \cdot \chi, \quad (10)$$

Note that although the prime symbol is used for Bishop's average skeleton stress, this should not be considered an effective stress variable; in fact, a second stress variable must be defined to adequately describe the behaviour under unsaturated conditions—e.g., suction [11,12]. If χ is properly selected to correspond to $\chi = 1$ upon full saturation ($S_r = 1.0$) and to $\chi = 0$ for dry states ($S_r = 0.0$), then Bishop's skeleton stress recalls Terzaghi's effective stress upon saturation which is a desirable feature for the unified description of saturated and unsaturated material states.

The Bishop's skeleton stress combined with common failure criteria for soils proves adequate when the interest focuses exclusively on the evolution of shear strength with partial saturation. This is supported by an ensemble of different studies [13–16], all of them suggesting that χ must be a function of S_r which ensures that $\chi = 1$ for $S_r = 1.0$ and $\chi = 0$ for $S_r = 0.0$, as previously discussed.

To this end, for the examined sliding block failure mechanism the shear resistance along the interface is described by the Mohr–Coulomb failure criterion combined with Bishop's skeleton stress:

$$\tau = c + \{\sigma + s \cdot \chi\} \cdot \tan\phi \quad (11)$$

where τ is the shear strength of the material described by the well known shear strength parameter cohesion (c) and angle of internal friction (ϕ). The failure criterion was then applied at the failure surface of the examined stability mechanism to calculate the shear resistance force (T) (see also Figure 2b), which can be calculated as (also see Appendix A):

$$T = c + (q + \gamma z) \cos^2\theta \cdot \tan\phi + s \cdot \chi \cdot \tan\phi \quad (12)$$

Finally, the safety factor against sliding of the block can be evaluated as the ratio of the forces resisting potential sliding and those trying to destabilize the examined block in the direction of the x axis. After some algebraic calculations for the 2D failure mechanism, the Factor of Safety (FoS) can be calculated according to:

$$FoS = \frac{T}{F_x} = \frac{\frac{c}{\cos^2\theta} + \frac{s \cdot \chi \cdot \tan\phi}{\cos^2\theta} + (q + \gamma z) \tan\phi}{(q + \gamma z) \tan\theta} \quad (13)$$

2.3. Extension to 3D-Lateral Shear Resistance

The simple 2D translational slope failure mechanism presented hereinbefore and quantified through Equation (13) can be used to evaluate the stability of planar slope instabilities where failure extends enough to reasonably assume that stability can be evaluated by performing a “per running meter analyses” where a slice of the falling mass with a thickness of 1m at the centre of the failure area is isolated and studied. However, in many cases, slope failures have rather finite dimensions where the aforementioned assumption becomes problematic.

In such cases, the main shortcoming of the 2D mechanism is that it neglects the contribution of the shear resistance developing at the sides of the failing mass. Neglecting their contribution proves conservative and usually this is the justification accompanying the assumption of simple 2D slope stability methods in the design of slopes and cuts. However, this is not true when it comes to the back analyses of slope failures where neglecting the actual dimensions of the failure mass and the contribution of the lateral resistance can significantly hinder the outcome of the analyses (i.e., overestimation of soil shear strength parameters and/or suction contribution).

To this end, this section extends the discussed translational failure mechanism in the 3D domain by additionally considering the contribution of lateral resistance. For this, the geometry presented in Figure 3 is considered. The failing block has a width (b) which limits its lateral development, while the depth of the failure mass is (z) and the length is $l = 1$ m, which as a horizontal distance translates to $a = \cos \theta$, similar to the 2D mechanism.

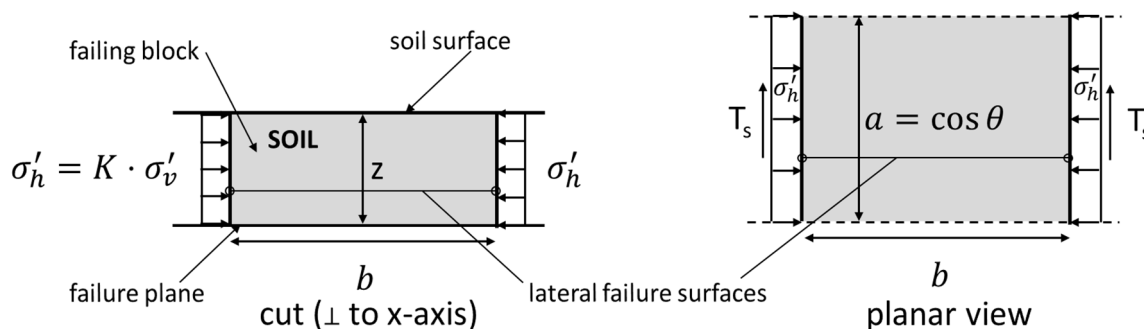


Figure 3. The 3D failure mechanism in cut and planar view.

To calculate the shear resistance T_s developing along each of the two lateral sides of the block, the Mohr–Coulomb failure criterion combined with Bishop’s average skeleton stress is used again. The horizontal stress at the two lateral interfaces is assumed to be equal to $\sigma'_h = K \cdot \sigma'_v$ where K is the coefficient of lateral earth pressure. Applying the lateral earth pressure coefficient to Bishop’s stress as opposed to total stress that other solutions assume (i.e., [1]) makes the derived solution applicable under positive pore water pressure regimes as well, while recent experimental evidence on soil anisotropy and partial saturation [17] also support such an assumption. The vertical Bishop’s skeleton stress is calculated in the middle of the depth (z) as:

$$\sigma'_v = \sigma_v + s \cdot \chi = q + \gamma \cdot \frac{z}{2} + s \cdot \chi \tag{14}$$

and the corresponding horizontal stress as:

$$\sigma'_h = K \cdot \sigma'_v = K \cdot q + K \cdot \gamma \cdot \frac{z}{2} + K \cdot s \cdot \chi \tag{15}$$

The stress as calculated in the middle of the layer is assumed uniform along the lateral sides of the excavation and the shear strength of the soil is then calculated as:

$$\tau_s = c_s + \sigma'_h \cdot \tan \phi_s \tag{16}$$

where c_s and ϕ_s are the cohesion and frictional resistance, respectively, along the lateral sides of the failure block. They are assumed to be different from their soil counterparts in favour of generality of the solution, by allowing different shear strength parameters to be assigned to the lateral resistance. Having defined the shear strength along the two lateral sides, we can calculate the corresponding shear resistance, where after some algebraic calculations (see Appendix B) the following expression is derived:

$$T_s = c_s \cdot z \cdot \cos \theta + K \cdot q \cdot z \cdot \cos \theta \cdot \tan \phi_s + K \cdot \gamma \cdot \frac{z^2}{2} \cdot \cos \theta \cdot \tan \phi_s + K \cdot s \cdot \chi \cdot z \cdot \cos \theta \cdot \tan \phi_s \tag{17}$$

Finally, using the additional resistance along the sides of the 3D mechanism, the safety factor against sliding is reformulated:

$$FoS = \frac{T + \frac{2T_s}{b}}{F_x} \tag{18}$$

Note that the additional resistance at the two sides ($2T_s$) is normalized over the width (b) of the block to combine it mathematically with the already determined resistance T and action F_x for the 2D mechanism. Finally, by using Equations (8), (12) and (17) to substitute for F_x , T and T_s , respectively, in Equation (18), we can calculate that the Factor of Safety (FoS) against sliding for the 3D mechanism as:

$$FoS = \frac{\frac{c}{\cos^2\theta} \left(1 + \frac{2\rho_c \cos\theta}{b}\right) + \frac{s\chi \tan\phi}{\cos^2\theta} \left(1 + \frac{2\rho_\phi K_z \cos\theta}{b}\right) + q \cdot \tan\phi \left(1 + \frac{2\rho_\phi K_z}{b \cdot \cos\theta}\right) + \gamma z \cdot \tan\phi \left(1 + \frac{\rho_\phi K_z}{b \cdot \cos\theta}\right)}{(q + \gamma z) \cdot \tan\theta} \quad (19)$$

In Equation (19), and in order to obtain a more elegant solution, the shear strength parameters used for the resistance along the inclined failure surface and along the sides of the block are correlated using the following factors:

$$\rho_s = \frac{c_s}{c} \quad (20)$$

$$\rho_\phi = \frac{\tan\phi_s}{\tan\phi} \quad (21)$$

3. Evaluation Using an Actual Case

To evaluate the planar slope stability mechanism previously presented and to demonstrate the potential importance of lateral resistance in analysing slope instabilities, the results from the Ruedlingen full scale experiment [1,18] will be used and compared with the predictions of the proposed stability mechanism.

3.1. The Ruedlingen Full Scale Experiment

The Ruedlingen full scale field test [1,18] was performed to study the response of a steep forested slope, subjected to artificial intense rainfall within the context of the multidisciplinary research programme on the “Triggering of Rapid Mass Movements in steep terrain” (TRAMM). The experiment was carried out in northern Switzerland in a forested area near Ruedlingen village. The selected experimental site is located on the east-facing bank of the river Rhine, with an average slope angle of approximately 38° . An orthogonal area, with a length of 35 m and a width of 7.5 m, was instrumented with a wide range of devices including earth pressure cells, piezometers, tensiometers, time domain reflectometers (TDRs), and acoustic and temperature sensors, organized in clusters, as seen in Figure 4b. A landslide triggering experiment was conducted in March 2009 where the slope was subjected to artificial rainfall with an average intensity of 20 mm/h at the upper one-third (approximately) of the slope and with 7 mm/h in the remaining lower part leading to a shallow slope failure after 15 h.

The failure concentrated at the upper part of the instrumented area (see Figure 4b) and extended within a surficial layer of a medium to low plasticity (average PI $\sim 10\%$) silty sand (ML) [19]. The developed failure mechanism can be characterized as a surficial planar failure. The mobilized area had a length of ~ 17 m, a width of ~ 7 m while the failure surface can be practically assumed to be parallel to both the soil surface and the underlying soil–bedrock interface with its maximum depth exciding 1 m [18]. This soil layer rests on top of a fissured Molassic bedrock (sandstone and marlstone—see Figure 4a) [20,21]. Sitarenios et al. [9] numerically analysed the triggered slope instability and, by combining field measurements with numerical results, they concluded that failure happens under saturated conditions and is triggered by water exfiltration from the bedrock which results in considerable pore water pressure build-up at the soil–bedrock interface.

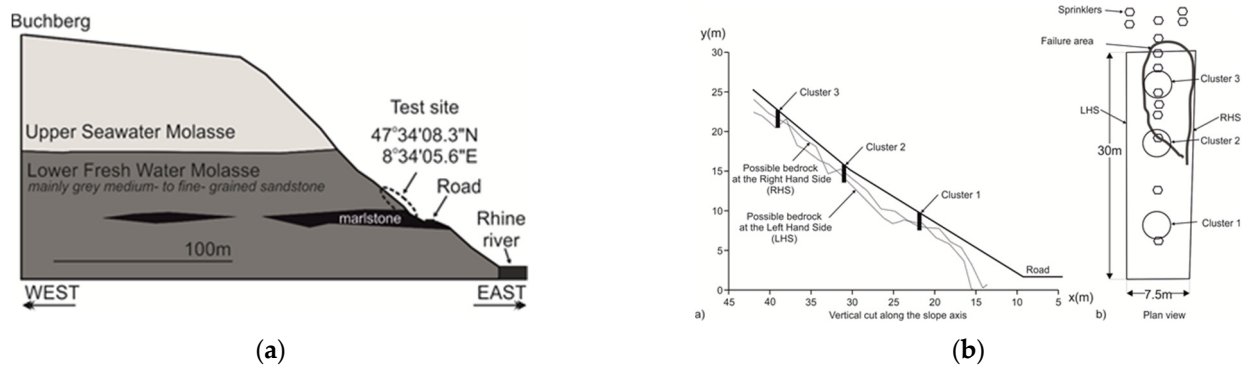


Figure 4. (a) Geomorphology of the greater experimental area (after [20]); (b) a schematic of the bedrock topography and of the instrumented area of the experiment (after [22]).

3.2. 2D Solution—Neglecting Lateral Resistance

In this section, the proposed limit equilibrium mechanism is used to evaluate the stability of the Ruedlingen slope by neglecting any contribution of lateral resistance or, in other words, by assuming an infinite failure mechanism perpendicular to the examined plane. When utilizing the mechanism, it is important to first establish the hydraulic and mechanical parameters of the Ruedlingen soil; to enable comparison of the results with the study of Sitarenios et al. [9], the same experimental data will be examined and similar assumptions will be put forward.

Starting with the hydraulic behaviour and according to what was previously discussed, calculation of the soil shear strength under unsaturated conditions necessitates knowledge of the degree of saturation as the latter is the most frequently made assumption for parameter (χ). To calculate the degree of saturation and thus parameter (χ), the Water Retention Model (WRM) of Equation (22) is used where s is the suction level, b_w is a model parameter controlling the shape of the reproduced Water Retention Curve (WRC) and $S_{r,max}$ and $S_{r,min}$ are the maximum and residual degrees of saturation, respectively. It is the a Van Genuchten type WRM [23] further including dependence of the behaviour of the void ratio ($e = n / (1 - n)$) through parameter P , as described in Equation (23), where P_0 and n_0 are reference values and parameter a_w controls the rate of change of the WRC with the void ratio.

$$\chi = S_r = S_{r,res} + (S_{r,max} - S_{r,res}) \left[1 + \left(\frac{s}{P} \right)^{\frac{1}{1-b_w}} \right]^{-b_w} \quad (22)$$

$$P = P_0 \cdot \exp[a_w(n_0 - n)] \quad (23)$$

It should be highlighted that the water retention behaviour is key to the accurate representation of the unsaturated shear strength. Consequently, in case of significant hysteresis in the water retention behaviour, attention must be given to the utilization of this branch of the curve (drying vs. wetting) which best represents the physically analysed problem. This study addresses a wetting problem (rainfall water infiltration) and, in this respect, the water retention behaviour is calibrated based on a set of suction controlled wetting laboratory tests [24]. The calibrated behaviour can be seen in Figure 5a and the parameters used are shown in Table 1. Figure 5b shows the WRC curve that is used in the analyses, which corresponds to an initial void ratio of $e = 0.9$ as this has been measured in the field and also used in previous studies [9]. It is accompanied by the evolution of the $s \cdot S_r$ term which in fact reflects the increase in the shear strength of the material with suction.

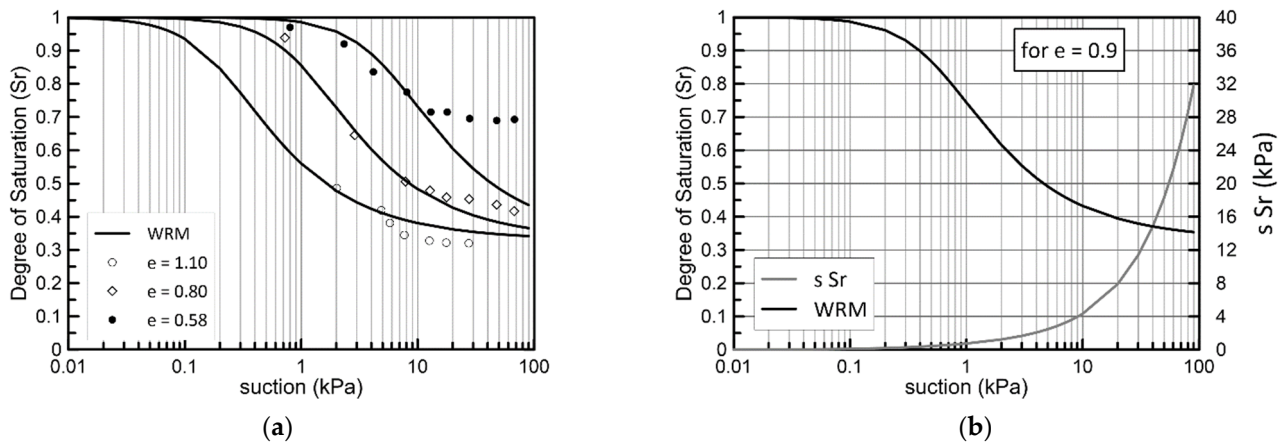


Figure 5. (a) The calibrated Water Retention Model (WRM) (laboratory data from [24]); (b) the Water Retention Curve (WRC) used in the analyses with the corresponding evolution of the $s \cdot S_r$ term.

Table 1. Ruedlingen WRM parameters used in this study.

Parameter	Value	Parameter	Value
P_0 (kPa)	0.65	α	21.0
b_w	0.4	n_0	0.47
$S_{r,max}$	1.0	$S_{r,min}$	0.33

With the WRM calibrated, Equation (11) is used to calculate the safety factor of the Ruedlingen slope under different combinations of suction and slope heights. With respect to the shear strength parameters involved in Equation (11), cohesion is set to zero ($c = 0$) and the friction angle equal to $\phi = 32$ [9,19], while the unit weight (γ) of the slope follows the evolution of saturation through Equation (1), with specific gravity equal to $G_s = 2.65$. Finally, the inclination of the failure surface is set equal to the average inclination of the slope ($\theta = 38$) [1] and no surcharge is considered on the soil surface ($q = 0$).

Figure 6 presents the results of a parametric study. Figure 6a portrays the evolution of the FoS with suction for various slope heights ranging from 0.5 to 2.75 m. The reason why the height of the slope is handled parametrically is related to the in situ variability of the thickness of the soil layer which was found, in general, to range from 0.5 to 4.5 m [18,20], while in the part of the slope where failure occurred the variation was smaller, with depths up to 2.75 m. In Figure 6b, similar results are presented with depth in the horizontal axis and the various curves represent different suction levels from zero (0) up to 10 kPa, following the in situ initial suction values as those have been reported in [18].

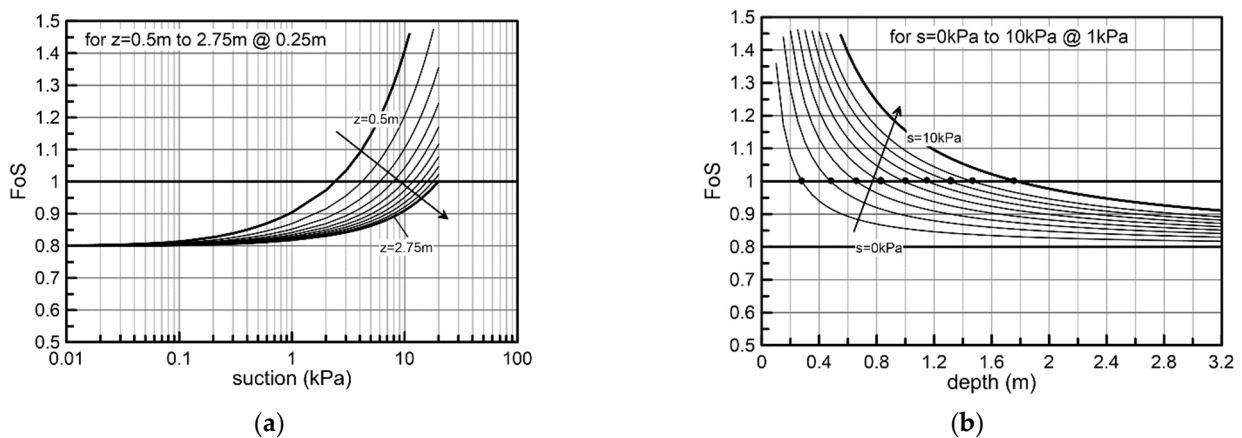


Figure 6. (a) Evolution of Factor of Safety (FoS) with suction for different slope heights; (b) evolution of FoS with slope height for different suction levels; results from a 2D mechanism (no lateral resistance).

The results of Figure 6 clearly demonstrate the dominant effect that partial saturation can have on stabilizing a planar slope. It is characteristic that when no suction is present ($s = 0$), a cohesionless slope ($c = 0$) has a safety factor which follows the $\frac{\tan(\phi)}{\tan(\theta)}$ ratio; the latter, for the examined slope geometry and soil shear strength is equal to $\frac{\tan(32)}{\tan(38)} = 0.8$. In both Figure 6a,b, it can be observed that even a small suction increase significantly alters stability conditions with various combinations of suction and slope heights exhibiting stable behaviours ($\text{FoS} \geq 1$).

To better understand this interplay between the height of the slope and suction, Figure 7 presents stability charts correlating the two quantities, with suction represented by the horizontal axis and slope height by the vertical axis, respectively. Figure 7a suggests that there is an almost linear relation between the increase in depth and the required increase in suction for the slope to remain stable ($\text{FoS} > 1$), while in Figure 7b the same relation is presented using a logarithmic scale with suction. Figure 7b helps to understand that the increase in the stable slope height with suction in fact follows the trend of the increase in the shear strength with suction as the latter is controlled by the increase in the $s \cdot S_r$ term in Figure 5b.

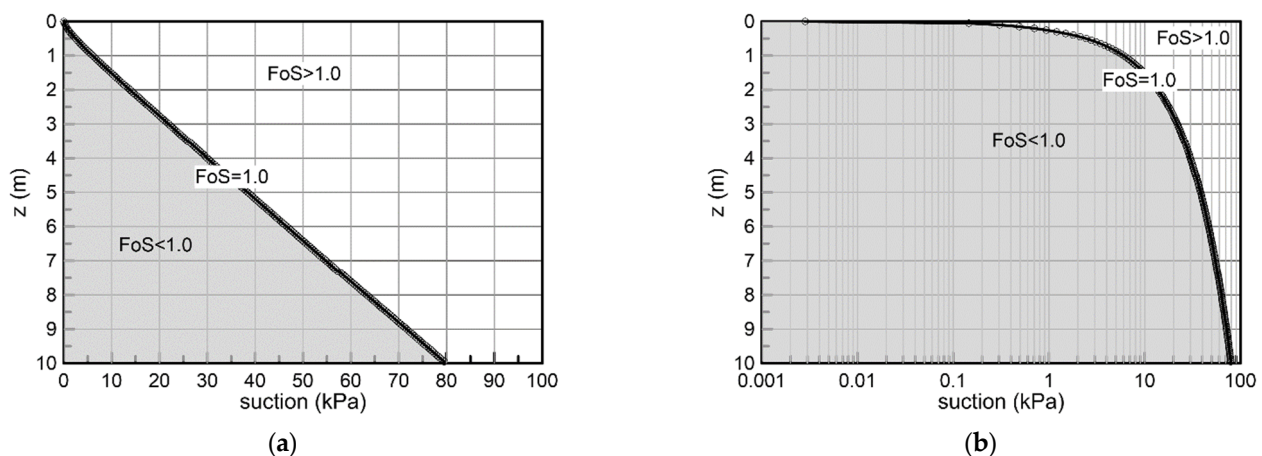


Figure 7. Stability chart; (a) stable vs. unstable suction and slope height combinations; (b) same as (a) in a semilogarithmic plot; results from a 2D mechanism (no lateral resistance).

Examining the stability chart of Figure 6 in relation to the observed behaviour during the Ruedlingen field experiment, it seems that the suggested evolution of stability with suction and slope height does not match the observed behaviour. If we consider an average slope height of 1.5 to 2 m, Figure 7 suggests that a minimum suction value of 10 to 15 kPa is required for stability. This may partially explain why the slope remains stable under the initial hydraulic regime which suggests a value of around 10 kPa, but at the same time it is obvious that even the smallest decrease in suction should cause failure. However, both in situ measurements [1] and numerical analyses [9] clearly indicate that even complete loss of suction is not enough to trigger the Ruedlingen failure. In this respect, it seems reasonable to assume that additional factors contribute to stability with respect to those examined with the present 2D failure mechanism.

3.3. 3D Solution—Including Lateral Resistance

Lateral resistance can be one of the factors contributing to improved stability conditions with respect to those of Figure 7. To consider the effect of lateral resistance in the examined problem, the analysis of the previous section is repeated by additionally considering the lateral resistance at the two sides of a failing block with a width equal to $b = 7.5$ m. For the side resistance, the same friction angle as for the soil–bedrock interface is assumed ($\rho_\phi = 1.0$), while for the lateral earth pressure coefficient an arbitrary value of $K = 0.5$ is chosen, close to the value suggested by Jaky's formula for $\phi = 32 \Rightarrow K = 1 - \sin 32 = 0.47$.

Figure 8 presents results similar to those of Figure 6; however, Figure 8 includes the additional contribution of lateral resistance. The results clearly demonstrate the beneficial effect of lateral resistance in increasing FoS under given combinations of slope height and suction. It is interesting to observe that Figure 8a seems to suggest that the effect of suction in improving stability conditions becomes less profound as the slope height increases. Moreover, Figure 8b indicates that under relatively small slope height values (i.e., less than 0.6 m), the influence of suction is quite significant, while as the slope height increases its effect becomes less profound, reaching a minimum for a given depth and then slightly increasing again.

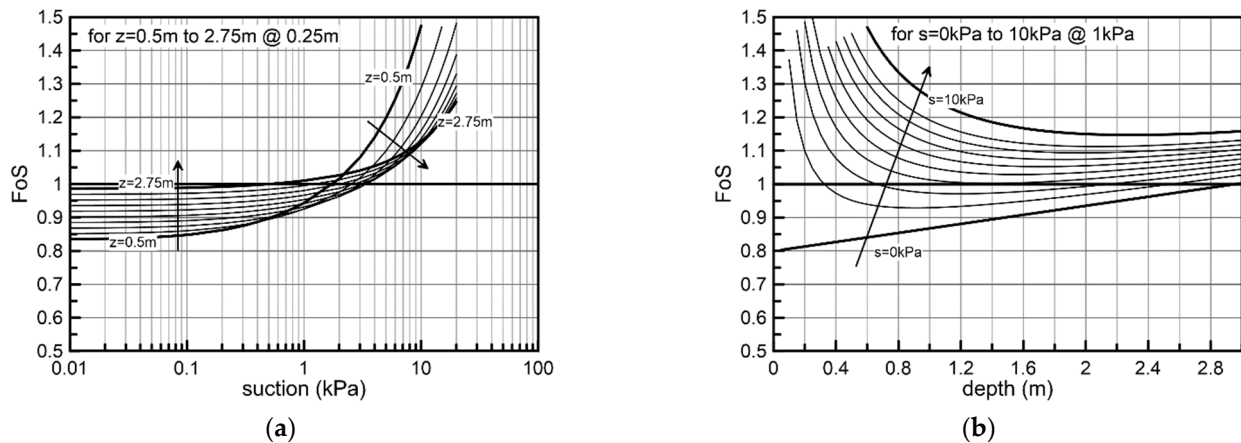


Figure 8. (a) Evolution of FoS with suction for different slope heights; (b) evolution of FoS with slope height for different suction levels; results from a 3D mechanism (with lateral resistance).

This effect is more profound in the results shown in Figure 9, presenting a stability chart similar to Figure 7 with the addition of lateral resistance. It is observed that as the height of the slope increases, positive pore water pressure values are needed to cause instability. Qualitatively, this trend in behaviour is much better aligned with the behaviour of the Ruedlingen slope, where failure happened following considerable water pressure build-up which reduced the available shear strength at the soil–bedrock interface. Moreover, both postfailure in situ observations and numerical results suggest that the depth of the failure surface ranged from 1.0 to 2.0 m. This is in good agreement with Figure 9, where within the same range of z values, the stability chart exhibits a peak coinciding with the most unfavourable stability conditions for the given assumptions.

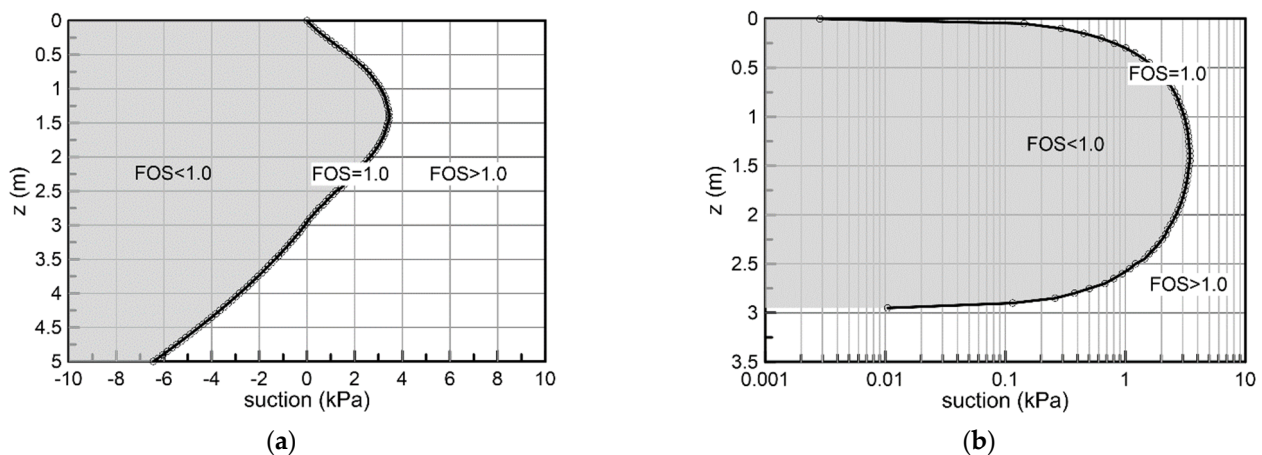


Figure 9. Stability chart; (a) stable vs. unstable suction and slope height combinations; (b) as (a) in a semilogarithmic plot; results from a 3D mechanism (with lateral resistance).

However, from a quantitative perspective and within the same range of slope heights, the required suction for stability suggests that the slope should have failed before reaching full saturation contrary to what was observed in situ. This discrepancy can be attributed to several factors which can result in better stability conditions than those described by the analysis used for this study. Amongst others, three of the most likely potential candidates for the different behaviours can be (a) the presence of some cohesion either due to fines or due to the contribution of vegetation and roots [25]; (b) a less extended mechanism in the third direction (smaller b) and (c) a different WRC. However, it should be recognized that the WRC can only affect the behaviour in the unsaturated regime and still cannot explain why a higher positive pore water pressure may be needed to trigger the instability.

3.4. 3D Solution—The Effect of Cohesion and 3D Mechanism Development

The previous section demonstrated how the inclusion of the lateral resistance in the analyses can justify an improvement of the stability conditions for the analysed Ruedlingen field experiment. However, it was not feasible to quantitatively approach the behaviour satisfactorily. As mentioned before, either the presence of cohesion or a narrower than assumed mechanism can serve as the most probable explanations and this hypothesis is put to test in this section.

To examine the effect of different assumptions regarding the aforementioned factors, a parametric analysis is conducted to check the sensitivity of the stability charts on the presence of cohesion (c) and on the width (b) of the 3D mechanism. Figure 10a presents how the stability curve differentiating between stable and unstable conditions changes with an increase in cohesion. Five different cohesion values, namely $c = 0, 1, 2, 3, 4$ and 5 kPa (from the blue to the red curve), are examined and the same cohesion values also control the lateral resistance by assuming that $\rho_c = 1.0$ (Equation (20)). The plotted charts indicate a significant contribution of cohesion to the stability conditions. Even the smallest nonzero value of $c = 1$ kPa is enough to justify a stable slope under the presence of the smallest suction and irrespective of its height. This is in accordance with the experimentally observed behaviour, while the presence of roots can justify even higher values of cohesion [25] which, if adopted (i.e., $c = 5$ kPa), can explain why significant pore pressures up to almost 10 kPa were needed in the soil–bedrock interface for failure to occur in the Ruedlingen experiment.

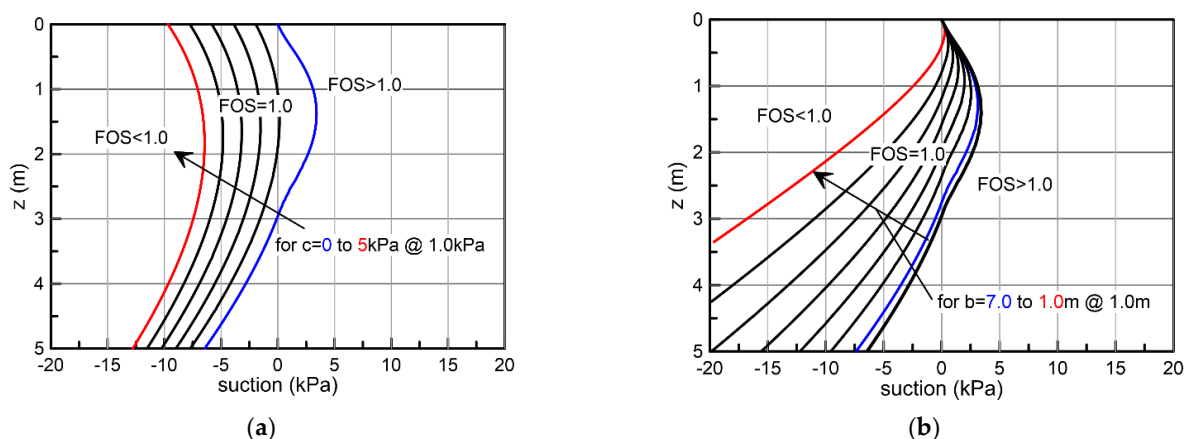


Figure 10. (a) Effect of cohesion on the stability chart; (b) effect of the 3D mechanism width on the stability chart; results from a 3D mechanism (with lateral resistance).

Figure 10b offers a similar discussion by explaining the effect of the width of the assumed mechanism. The main assumption put forward in the analyses presented hitherto is that the width of the mechanism is $b = 7.5$ m, coinciding with the width of the experimental area (dashed curve on Figure 9b). However, the in situ postfailure observations suggest that the failing mass had a smaller average width (see also Figure 4b), and the

results of Figure 10b indicate that such a reduction in the lateral development of the failure mechanism is quite beneficial for stability. In more detail, Figure 10b presents the evolution of the stability curves with the width of the mechanism, namely from $b = 7$ m down to $b = 1$ m (from the blue to the red curve). It is interesting that the effect of lateral development was qualitatively different compared to that of cohesion, with the slope height playing a key role. It is observed that as the slope becomes higher and the mechanism narrower, the effect of the lateral resistance on improving stability becomes higher. This is a clear reflection of the fact that the ratio of the area of the lateral side over the area of the soil–bedrock interface becomes higher, increasing the contribution of the side resistance and limiting the contribution of the failure plane resistance, thus progressively making the lateral resistance more and more dominant.

Regarding the in situ behaviour, it is clear that a narrower mechanism cannot explain the in situ behaviour alone; as for the slope height relevant to the Ruedlingen soil ($z = 1$ to 2 m) and the range of the lateral development of the mechanism ($b = 5$ to 7 m), the slope is still unstable, even though there is a noticeable improvement in stability conditions with respect to the reference scenario ($b = 7.5$ m). In this respect, the best candidate to justify the experimental behaviour is cohesion. From the results of Figure 10, it seems that reasonable assumptions regarding a small presence of cohesion in the order of $c = 3$ to 4 kPa, combined with a relatively smaller average mechanism $b = 5$ to 7 m, can explain very satisfactorily the experimentally observed behaviour during the Ruedlingen experiment, both qualitatively and quantitatively.

To test this assumption, four combinations of cohesion and slope width within the aforementioned range of values are finally analysed Figure 11b. In the same graph, the grey shaded area indicates the range of values of slope height and “suction” (negative suction values correspond to positive pore water pressure) most representative of the in situ failure conditions. In more detail, Figure 11a presents the failure mechanism (after [1]) where the average depth of the failure surface was more than 1 m. It also contains a plot of the evolution of the in situ and of the numerically determined pore water pressure at the failure area (after [9]) indicating that an average pore water pressure in the order of 5 kPa was present in the slope mass at failure. The very good match of the stability curves with the shaded area is a clear indication that the relatively simple 3D translational failure mechanism used in this study can provide a very good insight into the Ruedlingen failure.

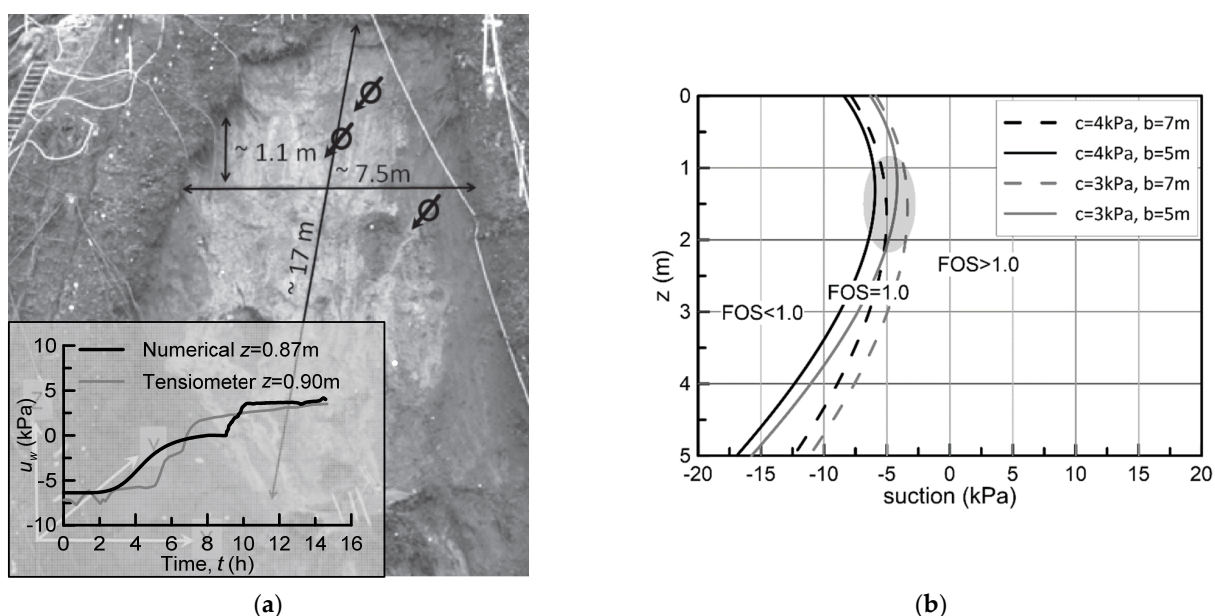


Figure 11. (a) The Ruedlingen slope failure (after [1]) and the evolution of pore water pressure in the slope mass (after [9]); (b) stability curves for different combinations of cohesion and slope widths which can accurately capture the observed instability (grey shaded area).

4. Conclusions

In this paper, a simplified limit equilibrium slope stability solution for infinite translational failure mechanisms was introduced. The solution uses Bishop's average skeleton stress to account for the increase in the shear strength under unsaturated conditions. It was extended in 3D dimensions by considering a potential limited lateral development of the failure mechanism by accounting for the lateral shear resistance that develops across the sides of the failing mass. Contrary to other similar attempts, the proposed solution assumes that the lateral earth pressure coefficient (K) describes the ratio of the horizontal over the vertical Bishop's stress and not only the net stress ratio. By doing so, the solution remains valid under fully saturated conditions where Bishop's average skeleton stress recalls Terzaghi's effective stress.

The mechanism was evaluated using a set of actual data from a full scale field experiment—the Ruedlingen artificial rainfall induced landslide. The proposed stability solution, despite its simplicity, can capture very satisfactorily the experimentally observed behaviour. Additionally, its simplicity and very limited calculation costs enable an easy evaluation of different scenarios with respect to slope geometries and soil parameters which can prove very useful in back analysis of slope failures. Such simple validated tools for the analyses of engineering problems under unsaturated conditions, formulated as a natural extension of similar classical soil mechanics solutions, are very important in facilitating a wider adoption of unsaturated mechanics in everyday geotechnical practice.

Author Contributions: Conceptualization, F.C.; Investigation, P.S.; Methodology, P.S.; Writing—original draft, P.S.; Writing—review & editing, F.C. All authors have read and agreed to the published version of the manuscript.

Funding: This research received no external funding.

Informed Consent Statement: Not applicable.

Data Availability Statement: Not applicable.

Conflicts of Interest: The authors declare no conflict of interest.

Appendix A

Starting from the Mohr–Coulomb criterion, Equation (11) is multiplied with the area of the failure surface, which is equal to $l = 1$ m, by 1 m for the distance perpendicular to the examined 2D problem (analyses per running meter). Thus, the shear resistance as a force is derived

$$T = c \cdot l + \{\sigma_n \cdot l + s \cdot \chi \cdot l\} \cdot \tan\phi \quad (\text{for } l = 1 \text{ m}) \quad \text{or} \quad (\text{A1})$$

$$T = c + N \cdot \tan\phi + s \cdot \chi \cdot \tan\phi \quad (\text{A2})$$

In Equation (A2), N represents the reaction force at the failure interface as this has been calculated with Equation (9) and so we can finally write:

$$T = c + (q + \gamma z) \cos^2 \theta \cdot \tan\phi + s \cdot \chi \cdot \tan\phi \quad (\text{A3})$$

Appendix B

In Equation (16), which represents the shear strength along the side of the examined mechanism, Bishop's average skeleton stress is described through Equation (15) to obtain:

$$\tau_s = c_s + \sigma'_h \cdot \tan\phi_s = c_s + \left(K \cdot q + K \cdot \gamma \cdot \frac{z}{2} + K \cdot s \cdot \chi \right) \tan\phi_s \quad (\text{A4})$$

Focusing on one side of the 3D mechanism, the shear strength above develops along the lateral side of the mechanism which is portrayed in Figure 1 by the light grey shaded

area. It is a parallelogram with an area equal to $z \cdot a = z \cdot \cos\theta$. Multiplying Equation (A4) with $z \cdot \cos\theta$, the shear resistance along the side is:

$$T_s = c_s \cdot z \cdot \cos\theta + \left(K \cdot q + K \cdot \gamma \cdot \frac{z}{2} + K \cdot s \cdot \chi \right) z \cdot \cos\theta \cdot \tan\phi_s \text{ or} \quad (\text{A5})$$

$$T_s = c_s \cdot z \cdot \cos\theta + K \cdot q \cdot z \cdot \cos\theta \cdot \tan\phi_s + K \cdot \gamma \cdot \frac{z^2}{2} \cdot \cos\theta \cdot \tan\phi_s + K \cdot s \cdot \chi \cdot z \cdot \cos\theta \cdot \tan\phi_s \quad (\text{A6})$$

References

1. Askarinejad, A.; Casini, F.; Bischof, P.; Beck, A.; Springman, S.M. Rainfall Induced Instabilities: A Field Experiment on a Silty Sand Slope in Northern Switzerland. *RIG Ital. Geotech. J.* **2012**, *3*, 50–71.
2. Tagarelli, V.; Cotecchia, F. The Effects of Slope Initialization on the Numerical Model Predictions of the Slope-Vegetation-Atmosphere Interaction. *Geosciences* **2020**, *10*, 85. [CrossRef]
3. Cotecchia, F.; Santaloia, F.; Tagarelli, V. Towards A Geo-Hydro-Mechanical Characterization of Landslide Classes: Preliminary Results. *Appl. Sci.* **2020**, *10*, 7960. [CrossRef]
4. Tang, A.M.; Hughes, P.N.; Dijkstra, T.A.; Askarinejad, A.; Brenčić, M.; Cui, Y.J.; Diez, J.J.; Firgi, T.; Gajewska, B.; Gentile, F.; et al. Atmosphere-Vegetation-Soil Interactions in a Climate Change Context; Impact of Changing Conditions on Engineered Transport Infrastructure Slopes in Europe. *Q. J. Eng. Geol. Hydrogeol.* **2018**, *51*, 156–168. [CrossRef]
5. Casini, F.; Minder, P.; Springman, S.M. Shear Strength of an Unsaturated Silty Sand. Unsaturated Soils. In Proceedings of the Fifth International Conference on Unsaturated Soils, Barcelona, Spain, 6–8 September 2010; pp. 211–216.
6. Springman, S.M.; Jommi, C.; Teysseire, P. Instabilities on Moraine Slopes Induced by Loss of Suction: A Case History. *Géotechnique* **2003**, *53*, 3–10. [CrossRef]
7. Zhang, L.L.; Zhang, J.; Zhang, L.M.; Tang, W.H. Stability Analysis of Rainfall-induced Slope Failure: A Review. *Proc. Inst. Civ. Eng. Geotech. Eng.* **2011**, *164*, 299–316. [CrossRef]
8. Ip, S.C.Y.; Rahardjo, H.; Satyanaga, A. Three-Dimensional Slope Stability Analysis Incorporating Unsaturated Soil Properties in Singapore. *Georisk Assess. Manag. Risk Eng. Syst. Geohazards* **2020**, 1–15. [CrossRef]
9. Sitarenios, P.; Casini, F.; Askarinejad, A.; Springman, S. Hydro-Mechanical Analysis of a Surficial Landslide Triggered by Artificial Rainfall: The Ruedlingen Field Experiment. *Géotechnique* **2021**, *71*, 96–109. [CrossRef]
10. Bishop, A.W.; Blight, G.E. Some Aspects of Effective Stress in Saturated and Partly Saturated Soils. *Geotechnique* **1963**, *13*, 177–197. [CrossRef]
11. Fredlund, D.G.; Morgenstern, N.R. Stress State Variables for Unsaturated Soils. *J. Geotech. Geoenviron. Eng.* **1977**, *103*, 447–466.
12. Gens, A. Soil–Environment Interactions in Geotechnical Engineering. *Géotechnique* **2010**, *60*, 3–74. [CrossRef]
13. Alonso, E.E.; Pereira, J.M.; Vaunat, J.; Olivella, S. A Microstructurally Based Effective Stress for Unsaturated Soils. *Geotechnique* **2010**, *60*, 913–925. [CrossRef]
14. Tarantino, A. A Possible Critical State Framework for Unsaturated Compacted Soils. *Geotechnique* **2007**, *57*, 385–389. [CrossRef]
15. Fredlund, D.G.; Xing, A.; Fredlund, M.D.; Barbour, S.L. The Relationship of the Unsaturated Soil Shear Strength to the Soil–Water Characteristic Curve. *Can. Geotech. J.* **1996**, *33*, 440–448. [CrossRef]
16. Vanapalli, S.K.; Fredlund, D.G.; Pufahl, D.E.; Clifton, A.W. Model for the Prediction of Shear Strength with Respect to Soil Suction. *Can. Geotech. J.* **1996**, *33*, 379–392. [CrossRef]
17. Al-Sharrad, M.A.; Gallipoli, D.; Wheeler, S.J. Experimental Investigation of Evolving Anisotropy in Unsaturated Soils. *Geotechnique* **2017**, *67*, 1033–1049. [CrossRef]
18. Askarinejad, A. Failure Mechanisms in Unsaturated Silty Sand Slopes Triggered by Rainfall. 2015. Available online: https://books.google.com.hk/books?hl=en&lr=&id=dlsBCwAAQBAJ&oi=fnd&pg=PP1&dq=Failure+Mechanisms+in+Unsaturated+Silty+Sand+Slopes+Triggered+by+Rainfall&ots=Lfw48yZeTp&sig=g36q8g2JoyVjJ_IA8Z0w4NLDq-c&redir_esc=y#v=onepage&q=Failure%20Mechanisms%20in%20Unsaturated%20Silty%20Sand%20Slopes%20Triggered%20by%20Rainfall&f=false (accessed on 27 January 2021).
19. Casini, F.; Jommi, C.; Springman, S. A Laboratory Investigation on an Undisturbed Silty Sand from a Slope Prone to Landsliding. *Granul. Matter* **2010**, *12*, 303–316. [CrossRef]
20. Brönnimann, C.; Tacher, L.; Askarinejad, A.; Kienzler, P.; Springman, S.M. Pore Water Pressure Modelling in a Rainfall Triggered Shallow Landslide. In Proceedings of the 7th Swiss Geoscience Meeting, Neuchâtel, Switzerland, 20–21 November 2009; pp. 280–281.
21. Springman, S.; Askarinejad, A.; Casini, F.; Friedel, S. Lesson Learnt from Field Tests in Some Potentially Unstable Slopes in Switzerland. *Acta Geotech. Slov.* **2012**, *1*, 5–29.
22. Askarinejad, A.; Casini, F.; Kienzler, P.; Teysseire, P.; Springman, S.M. Mountain Risks: Two Case Histories of Landslides Induced by Artificial Rainfall on Steep Slopes. In *Mountain Risks: Bringing Science to Society, Proceedings of the “Mountain Risks” International Conference, Firenze, Italy, 24–26 November 2010*; CERIG Editions; 2010; Available online: https://art.torvergata.it/handle/2108/93850#YBE-mU_itPY (accessed on 27 January 2021).
23. van Genuchten, M.T. A Closed-Form Equation for Predicting the Hydraulic Conductivity of Unsaturated Soils. *Soil Sci. Soc. Am. J.* **1980**, *44*, 892–898. [CrossRef]

-
24. Casini, F. Deformation Induced by Wetting: A Simple Model. *Can. Geotech. J.* **2012**, *49*, 954–960. [[CrossRef](#)]
 25. Fraccica, A.; Romero, E.; Fourcaud, T.; Sondon, M.; Gandarillas, L. Tensile Strength of a Vegetated and Partially Saturated Soil. *E3S Web Conf.* **2020**, *195*. [[CrossRef](#)]